Journal of Materials Chemistry A

ROYAL SOCIETY OF CHEMISTRY

PAPER

View Article Online
View Journal

Check for updates

Cite this: DOI: 10.1039/d6ta00808a

Nanocomposites with tunable dielectric properties: $BaTiO_3$ loaded cellulose nanocrystal-liquid crystalline polymers

Patrick K. Njenga,[a] Ning Guo,[b] Haotian Long,[c] Dennis M. Ndaya,[b] Akram H. Alhadainy,[bd] Chinedum O. Osuji,[c] Yang Cao[be] and Rajeswari M. Kasi *[ab]

Dielectric nanocomposites are emerging as next-generation energy storage materials due to their applicability in advanced electronics, renewable energy systems, and electric vehicles. In this work, we report the rational molecular design, synthesis, and structure–property investigation of a $BaTiO_3$/cellulose nanocrystal (CNC)-liquid crystal polymer (LCP) nanocomposite with enhanced dielectric performance. The hybrid platform integrates $BaTiO_3$ nanoparticles dispersed within a cyanobiphenyl-based polyacrylate matrix (PAACB12-r-PAA), followed by *in situ* interlocking with CNCs. This biomaterial-supported anisotropic system, exploits both the permanent dipole of smectic cyanobiphenyl liquid crystalline mesogens and ordering of CNC-LC materials to induce hierarchical self-assembly and promote strong dielectric responses. Films are fabricated through hot-pressing at the liquid crystalline transition temperature (T_{LC}), followed by rapid quenching to lock in the alignment. We systematically investigate the influence of processing parameters such as $BaTiO_3$ concentration, LCP alignment, and thermal treatment on dielectric behavior. Temperature-controlled small-angle X-ray scattering (TSAXS), broadband dielectric spectroscopy, and microscopy are employed to correlate mesophase orientation, dispersion quality, and molecular interactions with the dielectric constant, breakdown strength, energy density, and dielectric loss. Our findings reveal that the liquid crystalline matrix not only enhances $BaTiO_3$ dispersion and interfacial polarization but also facilitates structural ordering that improves the composite's dielectric performance. The permanent dipoles within the LCP matrix further augment polarization *via* Ti^{4+} displacement from the O^{2-} octahedra in $BaTiO_3$, offering tunable dielectric enhancement. This work establishes a general strategy for designing multifunctional dielectric nanocomposites by integrating mesogen alignment, nanofiller anisotropy, and optimized processing to achieve tunable dielectric performance for advanced electronic applications.

Received 27th January 2026
Accepted 5th April 2026

DOI: 10.1039/d6ta00808a

rsc.li/materials-a

Introduction

Dielectric nanocomposites have attracted significant interest as next-generation energy storage materials due to their broad applications in advanced electronics, renewable energy systems, and electric vehicles.[1–3] Among these, ceramic–polymer nanocomposites, especially those combining barium titanate ($BaTiO_3$) with functional polymer matrices, stand out for their tunable electrical, mechanical, and structural properties.[4–6] One such promising platform integrates $BaTiO_3$ with liquid crystal polymers (LCPs), which offer molecular-level ordering, anisotropic dielectric responses, and field-induced alignment.[7–10]

$BaTiO_3$ is an energy storage ceramic with a high dielectric constant and reversible polarization, making it ideal for capacitors, sensors, and transducers.[11–13] However, its use in practical applications is hindered by brittleness, high density, temperature sensitivity, low dielectric strength, and poor processability.[14–17] Embedding $BaTiO_3$ within flexible polymeric matrices is hypothesized to improve the mechanical robustness and processing characteristics, while retaining or even enhancing dielectric performance.[6,18–20]

Organic dielectric polymers have been employed as dielectric materials due to their low-temperature and facile processability, impressive flexibility, corrosion resistance, excellent insulation properties, lightweight nature, and good thermal stability.[14,21,22]

[a]Department of Chemistry, University of Connecticut, Storrs, CT 06269, USA. E-mail: rajeswari.kasi@uconn.edu; Tel: +1 (860)-486-4713
[b]Institute of Materials Science, University of Connecticut, Storrs, CT 06269, USA
[c]Chemical and Biomolecular Engineering, University of Pennsylvania, PA, 19104-639, USA
[d]Department of Biomedical Engineering, University of Connecticut, Storrs, CT 06269, USA
[e]Department of Electrical Engineering, University of Connecticut, Storrs, CT 06269, USA

In this category, biodegradable cellulose nanocrystals have gained increased interest due to their non-toxicity, renewability, high aspect ratio, adaptable surface chemistry, liquid crystallinity, and stiffness, making them a potential replacement for most synthetic dielectric polymers, which pose challenges to the environment.[11,23–25] Du *et al.* demonstrated the natural dielectric behavior of cellulosic biopolymers in A4 paper form, where the paper is adapted as an energy storage material with excellent wettability.[26–28] In a similar study, Jose and coworkers reported the temperature-dependent (30 °C to 100 °C) dielectric properties of CNC paper over a frequency range of 1 Hz to 10 MHz. Here, the authors established a temperature trend of the dielectric properties, proving the potential of CNCs as an environmentally benign energy storage material in flexible electronics.[29]

Other liquid crystalline polymers (LCPs), such as smectic cyanobiphenyl, present distinct advantages, such as a well-defined processing window governed by their liquid crystalline transition temperature (T_{LC}), intrinsic anisotropy, and stimuli-responsive molecular alignment, all of which can be tailored to enhance dielectric performance.[30–32] Interlocking these anisotropic smectic LC molecules with chiral nematic CNCs modifies the dielectric performance of the system.[32–34] The electric field-induced alignment of these polar structures enhances local polarization by facilitating Ti^{4+} displacement from the O^{2-} octahedra in $BaTiO_3$, thereby augmenting dipole formation and energy storage.[35–37]

While the dielectric properties of LCPs have been extensively studied, the use of broadband dielectric spectroscopy to investigate the effects of nanoparticles on the dynamics of LCPs with mesomorphic phases has received limited attention. In this study, we present dielectric spectroscopy results of a novel $BaTiO_3$/CNC-LCP nanocomposite. The incorporation of $BaTiO_3$ nanoparticles not only significantly enhances the dielectric constant but also suppresses the librational fluctuations of the 12-spacer cyanobiphenyl mesogen around the long molecular axis. Because $BaTiO_3$ does not establish a wetted interface with CNC-i-PAACB12-r-PAA, the nanoparticles act more as steric obstacles within the long-range ordered structure (whose formation is also facilitated by $BaTiO_3$) to hinder the motion of the mesogen. This constrained movement results in a slight increase in the liquid–crystal transition temperature, T_{LC1}, of the nanocomposite. These findings provide new insight into how inorganic fillers modulate the dielectric response of LCP-based nanocomposites.

Experimental

Materials

Barium titanate, $BaTiO_3$ (cubic), 4-dimethylamino pyridine, DMAP (99.0%), potassium carbonate (99%), acrylic acid (99%) and azobisisobutyronitrile, AIBN (98%), are purchased from Sigma Aldrich. 12-Bromo-1-dodecanol (95%) is provided by Lab Seeker Chemicals, while 4-cyano-4′-hydroxyphenyl is obtained from TCI America. Cytiva Life Sciences supplied standard-grade Whatman filter paper, while dimethyl formamide (99%) is purchased from Across Organics. 1-Ethyl-3-(3-dimethyl aminopropyl) carbodiimide hydrochloride, EDC·HCl (98.0%) and 1-butyl-3-methylimidazolium acetate (95%) are acquired from Oakwood Chemicals. Thermo Fisher Scientific supplied dichloromethane (98%) and dimethyl sulfoxide (99.0%).

Synthesis of $BaTiO_3$/PAACB12-r-PAA

$BaTiO_3$ nanoparticles and PAACB12-r-PAA were homogenously dispersed in THF by ultrasonication at room temperature for 1 h. The sonicated sample is dried over nitrogen and subsequently vacuum-dried to form $BaTiO_3$/PAACB12-r-PAA, as outlined in Scheme 1 below.

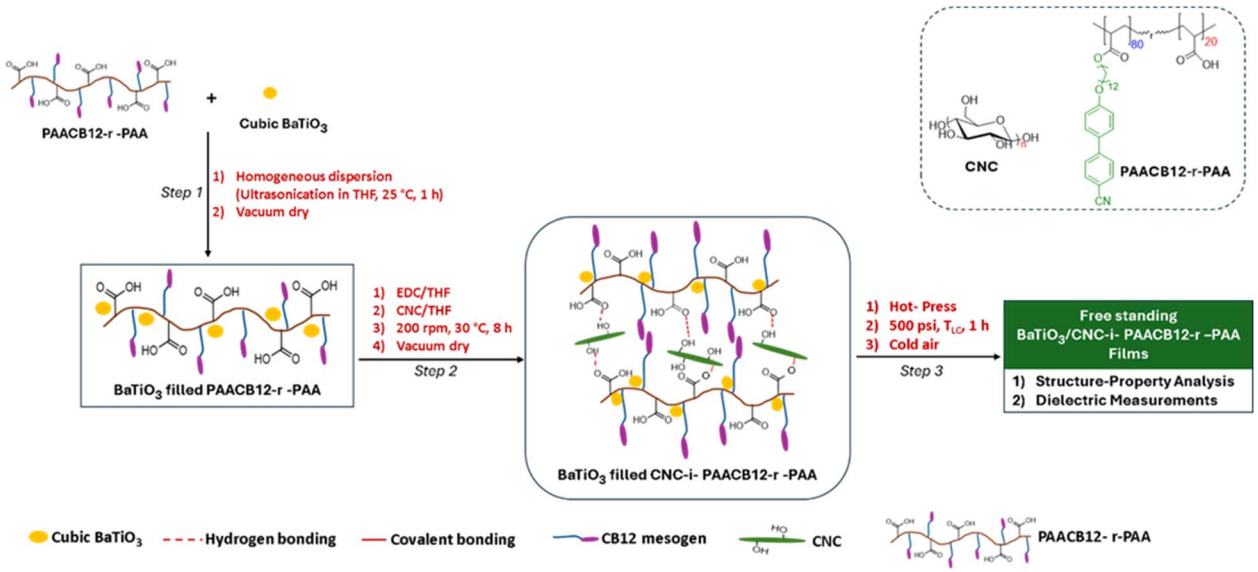

Scheme 1 Synthetic scheme for the formation of $BaTiO_3$/CNC-i-PAACB12-r-PAA nanocomposites for dielectric studies.

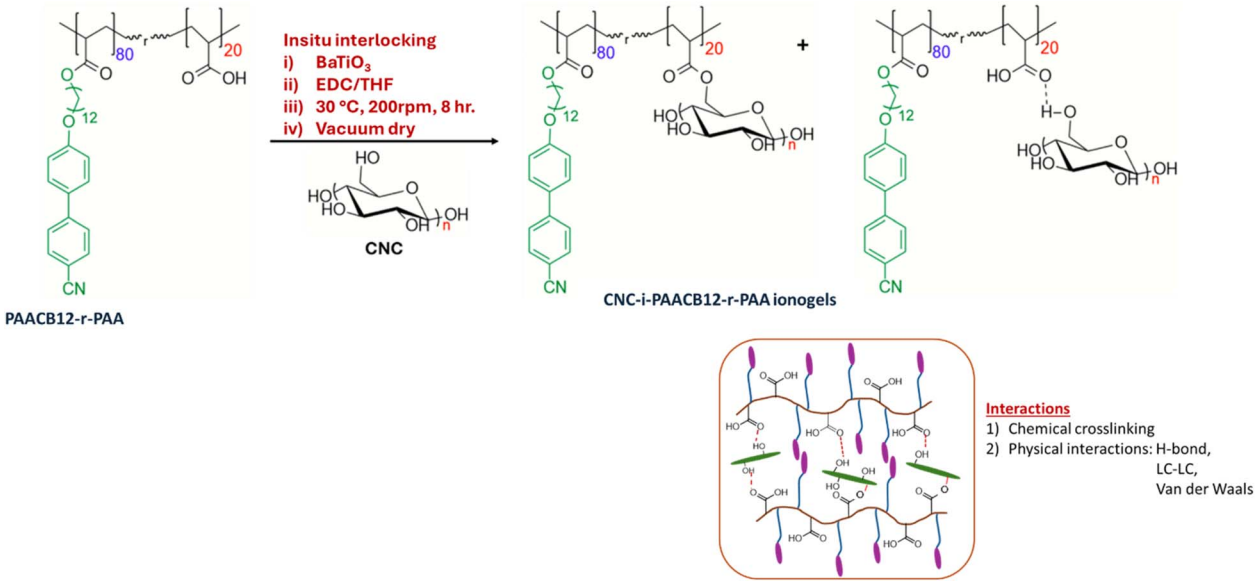

Scheme 2 Synthetic pathway showing dual network $BaTiO_3$/CNC-i-PAACB12-r-PAA nanocomposite gels using 40 wt% EDC in THF.

Table 1 Feed ratios for the PAACB12-r-PAA, CNC, EDC, and $BaTiO_3$ nanoparticles

Nanocomposite	PAACB12-r-PAA (mg)	CNC (mg)	$BaTiO_3$ (mg)	EDC (mg)	THF (mL)
CNC-i-PAACB12-r-PAA	80	20	0	40	1
$BaTiO_3$ (10 wt%)/CNC-i-PAACB12-r-PAA	80	20	41.6	40	1
$BaTiO_3$ (20 wt%)/CNC-i-PAACB12-r-PAA	80	20	83.2	40	1
$BaTiO_3$ (40 wt%)/CNC-i-PAACB12-r-PAA	80	20	166.4	40	1

Preparation of $BaTiO_3$/CNC-i-PAACB12-r-PAA nanocomposites

$BaTiO_3$/PAACB12-r-PAA is then interlocked *in situ* with CNCs *via* double interlocking chemistry, as shown in Scheme 2. The reactants (Table 1) are transferred to a clean, dry 50 mL round-bottomed flask equipped with a magnetic stir bar. 5 mL THF is added, and the flask is sealed with a rubber septum. The reaction mixture is purged with argon for 3 minutes and stirred in an oil bath at 0 °C for 2 hours. The temperature gradually increased to 30 °C, and the reaction was allowed to continue for a further 6 hours. The crude reaction mixture is then cooled and carefully transferred into a clean, dry scintillation vial and ultrasonicated at 25 °C for 1 hour for optimal dispersion. After complete sonication, the sample is vacuum-dried at room temperature overnight. Free-standing films were then prepared by hot-pressing the nanocomposite at the corresponding T_{LC} (for 1 hour), followed by cold-air quenching to induce hierarchical self-assembly. This enables phase alignment, essential for high-performance dielectric materials.[38–40] The synthetic scheme for the formation of $BaTiO_3$/CNC-i-PAACB12-r-PAA nanocomposite films is shown in Scheme 1.

Results and discussion

The system studied is a hybrid LCP consisting of an amphiphilic random copolymer, PAACB12-r-PAA, with relative degrees of polymerization of 80 for PAACB12 and 20 for PAA, as shown in Scheme 1. The backbone has cyanobiphenyl mesogens attached at the ends as side chains to a polyacrylate backbone, while the other unit contains free COOH groups that interlock/crosslink with CNCs.

Structural identification of the copolymer is performed using ^{1}H NMR, assessing the chemical shifts of the respective protons, while that of the hybrid LCP and the $BaTiO_3$-loaded nanocomposites is achieved by identifying the functional groups of the material using Fourier Transform Infrared (FTIR) spectroscopy.

Thermal analysis of the hybrid LCP and the nanocomposites is performed to understand thermal stability and phase transition behavior. Thermal gravimetric analysis (TGA) enables us to understand the decomposition profile of the material using the decomposition temperatures. The higher the decomposition temperature (T_d), the more thermally stable the material. TGA studies also inform us about the interaction of the hybrid LCP with $BaTiO_3$ and provide the range of temperatures over which DSC studies can be conducted. Differential Scanning Calorimetry (DSC) studies provide information on the phase transitions exhibited by the materials, such as melting temperatures (T_m), glass transition temperature (T_g), crystallization temperatures (T_c), liquid crystal transition temperatures (T_{LC}), and isotropic temperatures. We can leverage DSC studies

to investigate the interactions between CNCs and the copolymer in the formation of the hybrid LCP and the interaction of $BaTiO_3$ with the hybrid LCP when preparing the nanocomposites.

X-ray techniques, such as X-ray Diffraction (XRD) and Small-Angle X-ray Scattering (SAXS), can be employed to investigate the microstructure and self-assembly behavior of $BaTiO_3$-loaded CNC-cyanobiphenyl LCP hybrid nanocomposites. XRD scattering patterns reveal the crystallite sizes of $BaTiO_3$, CNC-i-PAACB12-r-PAA, and $BaTiO_3$/CNC-i-PAACB12-r-PAA nanocomposites. We can also assess the interfacial interactions of $BaTiO_3$ with the hybrid LCP (CNC-i-PAACB12-r-PAA) by monitoring changes in crystallinity symbolized by any shift or broadening in diffraction peaks. On the other hand, SAXS studies give information regarding the hierarchical ordering and periodicity of the hybrid LCP and the $BaTiO_3$-loaded nanocomposites. This helps us decipher the resultant mesophase during self-assembly. CNCs can also serve as alignment agents for PAACB12-r-PAA, which promotes ordered domains that enhance dielectric anisotropy.

Structure identification

The fundamental step in characterizing CNC-LCP nanocomposites is to conduct structural identification of the copolymer by assessing the chemical shifts of the respective protons in Nuclear Magnetic Resonance (NMR) spectroscopy, while that of the hybrid LCP and the $BaTiO_3$-loaded nanocomposites is achieved by identifying the functional groups of the material using Fourier Transform Infrared (FTIR) spectroscopy. Careful evaluation of these functional groups gives us information on dominant interactions between CNCs, LCPs, and $BaTiO_3$, which can then be correlated with the dielectric performance of the resultant nanocomposites.

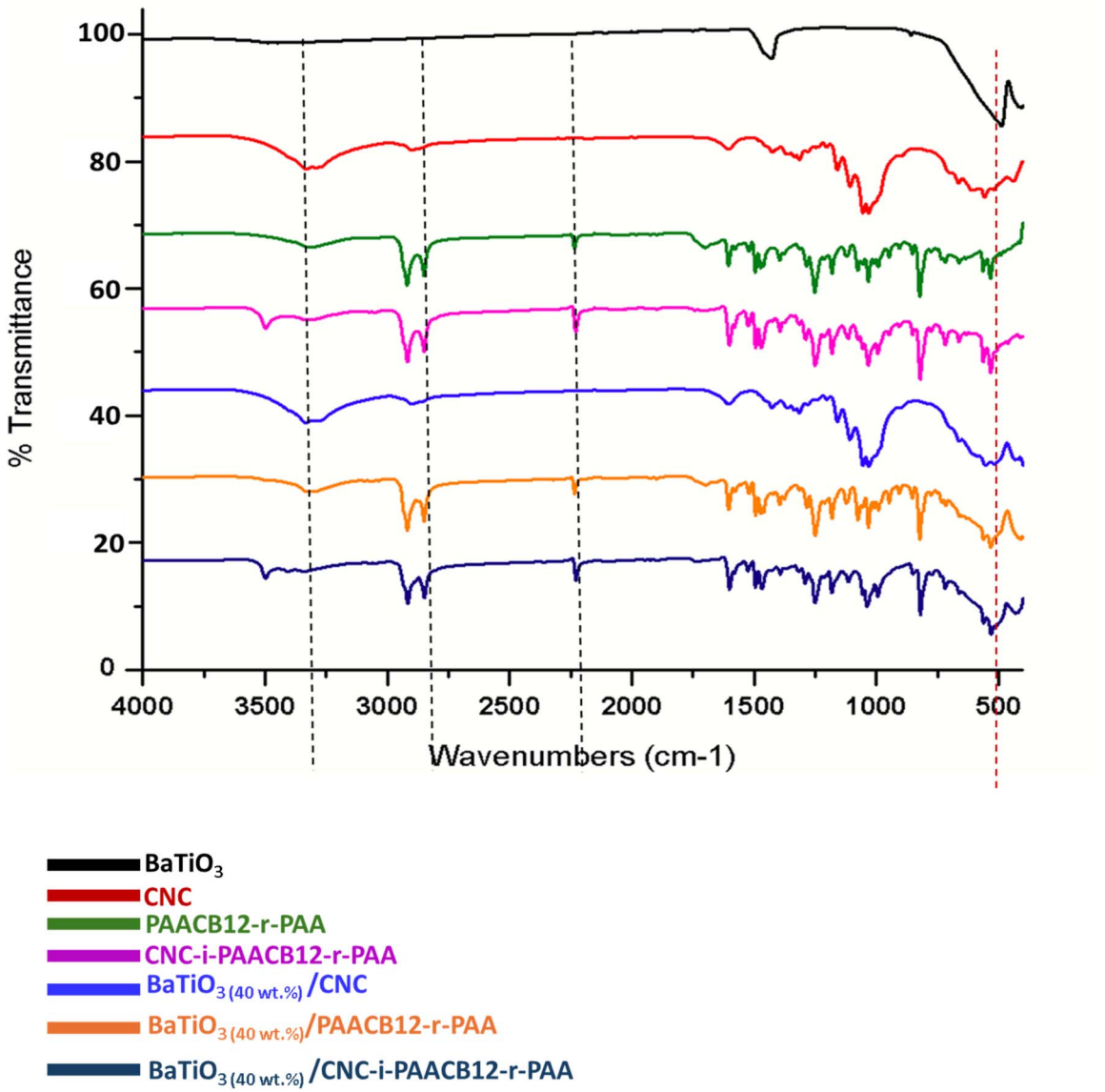

Fig. 1 Stacked FTIR results of copolymers, hybrid LCPs, and $BaTiO_3$/CNC-i-PAACB12-r-PAA nanocomposites.

Table 2 FTIR results for the $BaTiO_3$ nanoparticles, CNCs, copolymer, hybrid LCP, and $BaTiO_3$ nanocomposites

Functionality	Wavenumbers (cm^{-1})
C≡N	2229.53 (cyanobiphenyl LC)
C═O	1601.40
C–O	1288.56
O–H	3333.91, 3497.62
C–H	2849.60, 2917.50
Ti–O	**502.15 (perovskite)**

Successful formation of the cyanobiphenyl mesogen, acrylate monomer, and LC copolymer is characterized by ^{1}H NMR. For the AACB12 monomer, we observe a proton signal peak at 4.0 ppm that serves as the connection peak. In contrast, the signal peak between 6.0 and 6.5 ppm shows the presence of a double bond in the acrylate monomer, a polymerization site. Biphenyl protons appear at 7.1 ppm, 7.6 ppm, and 8.0 ppm, respectively. These peaks confirm the successful grafting of the CB12 mesogen onto the acrylate backbone, as shown in Fig. S2. The ^{1}H NMR spectrum for the copolymer shows the disappearance of the peaks at 6.0–6.5 ppm, indicating complete polymerization. We also observe an acidic proton signal at 12.0 ppm, which further confirms the success of copolymerization as seen in Fig. S3.

Formation of the hybrid LCP and $BaTiO_3$/CNC-i-PAACB12-r-PAA nanocomposite is further confirmed by FTIR studies. For instance, we observe a strong C≡N stretching band at 2235.2 cm^{-1}, C═O stretch at 1712.2 cm^{-1}, O–H at 3339.6 cm^{-1}, and C–O at 1287.3 cm^{-1} in the nanocomposite, as shown in Fig. 1 below. We monitor the surface modification of $BaTiO_3$ nanoparticles by comparing FTIR spectra of pure and modified $BaTiO_3$. FTIR spectra of neat $BaTiO_3$ show a prominent Ti–O bond stretching along the polar axis at 502.15 cm^{-1}, which corresponds to the symmetric stretching vibration of TiO_6 octahedra. This peak is important for monitoring any changes in the crystal structure after surface functionalization of $BaTiO_3$. The peak at 1435 cm^{-1} is considered an artefact corresponding to $BaCO_3$ impurities. $BaTiO_3$/CNC-i-PAACB12-r-PAA shows additional asymmetric vibrations at around 600 cm^{-1}, indicating distortion of the crystal symmetry of $BaTiO_3$. This distortion results from the interplay of the polar axis of $BaTiO_3$ with the permanent dipole in the LCP. Further studies on perturbation of the crystal structure after functionalization are performed using thermal and microstructural analyses, discussed in the next section below (Table 2).

Thermal analysis

To understand the thermal behavior of the materials, we conduct thermal analysis using thermogravimetric analysis (TGA) and differential scanning calorimetry (DSC).[41,42] TGA gives us information concerning the decomposition behavior of the material.[42,43] We establish a linear relationship between thermal stability and $BaTiO_3$ concentration in the nanocomposite, as confirmed by the increase in onset thermal decomposition temperature (T_d). All the materials are reported to be thermally stable within the range of DSC measurements. The TGA results for these materials are shown in Table S1 and Fig. 2 below.

Thermal transitions for the PAACB12-r-PAA copolymer, CNC-i-PAACB12-r-PAA, and $BaTiO_3$ (20 wt%)/CNC-i-PAACB12-r-PAA are probed by DSC as shown in Fig. 3. Samples are heated at a constant heating rate of 10 °C min^{-1} to 150 °C. The 1st heating cycle of each sample run is assumed to represent the artifact and thermal history present in the sample. The first cooling and second heating cycles are analyzed and reported as shown in Fig. 3. The PAACB12-r-PAA copolymer shows a prominent peak at 84.34 °C from the 1st cooling cycle and 97.99 °C in the 2nd heating cycle. The copolymer appears to be highly crystalline, thus masking the mobile nature of the CB12 mesogen. The 1st cooling DSC profile for CNC-i-PAACB12-r-PAA shows two distinct transitions: T_{LC} at 40.75 °C with an enthalpy requirement of 3.79 J g^{-1} and a T_C at 81.13 °C. Similar observations are made in 10 wt% nanocomposites with a T_{LC} at 42.26 °C and a T_C at 78.53 °C. Similar observations are made during the 2nd

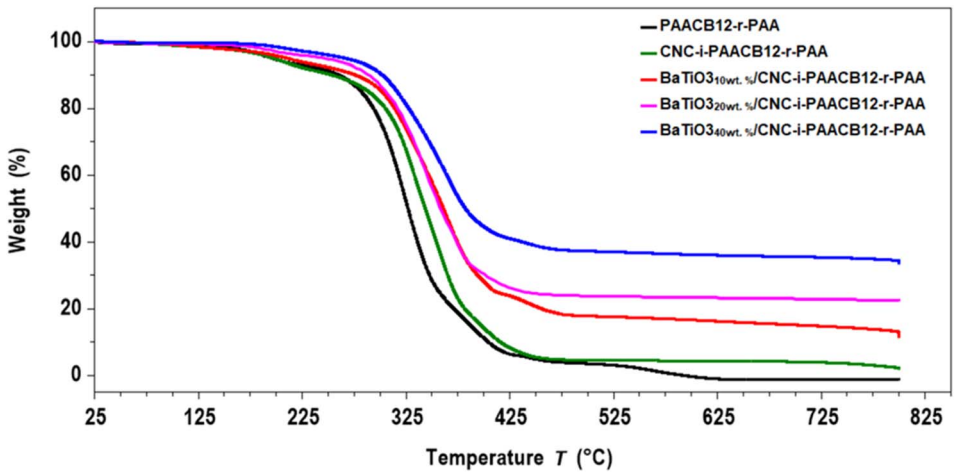

Fig. 2 TGA profiles for different nanocomposites.

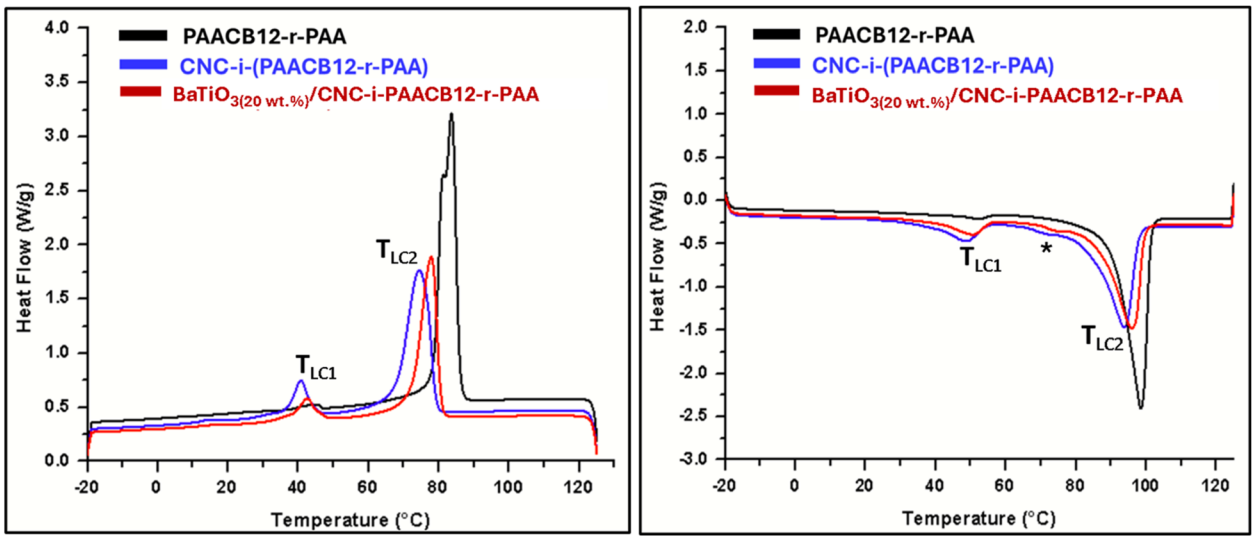

Fig. 3 1st cooling and 2nd heating cycles DSC thermograms for the copolymer, hybrid LCP and $BaTiO_3$ (10 wt%)/CNC-i-(PAACB12-r-PAA) nanocomposite.

heating cycle. Neat CNC and $BaTiO_3$ samples show no presence of thermal transitions, as shown in Fig. S4.

To gain insight into self-assembly and resultant mesomorphic structures, further studies of the hybrid LCP and $BaTiO_3$/CNC-i-PAACB12-r-PAA nanocomposites are conducted by small-angle X-ray scattering studies (SAXS).

Microstructure

We investigate the microstructural changes resulting from the integration of cubic $BaTiO_3$ into the CNC-i-PAACB12-r-PAA matrix using X-ray diffraction (XRD) studies. Fig. 4 shows the XRD profile for $BaTiO_3$ (40 wt%)/CNC-i-PAACB12-r-PAA, where the material shows biphasic behavior with the diffraction peaks traceable to PDF 79-2263, corresponding to cubic $BaTiO_3$ nanoparticles. Bragg's reflections 1, 2, 5, 6, and 8 are traceable to the CB12 mesogen and 3, 4, 7, and 9 are pertinent to CNCs. Peak fitting is performed using Origin software, where the obtained full width at half maximum (FWHM) helps us calculate the line broadening in radians. After obtaining the line broadening, we use the Scherrer equation to calculate the crystallite

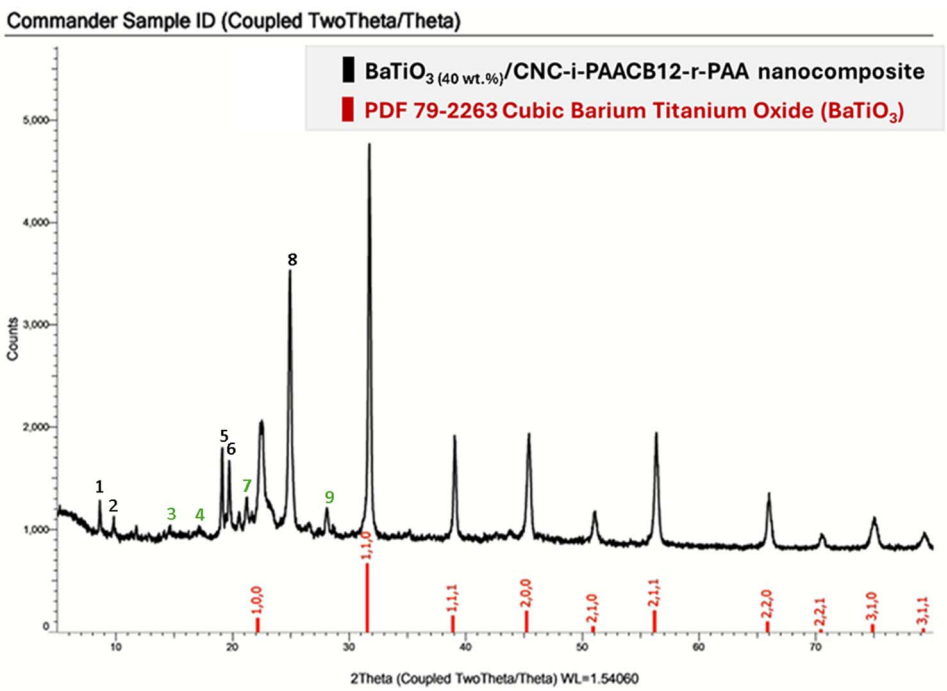

Fig. 4 XRD profile for the 40 wt% $BaTiO_3$ nanocomposite showing scattering peaks pertinent to cubic $BaTiO_3$, where Bragg's reflections indexed in green (3, 4, 7, and 9) are pertinent to CNCs, while those indexed in black (1, 2, 5, 6, and 8) are pertinent to the CB12 mesogen in the copolymer.

size of $BaTiO_3$ using the prominent peak, represented by the lattice parameters (110). The calculation of the crystallite size of $BaTiO_3$ is shown below.

$$D = \frac{K\lambda}{\beta\cos\theta}$$

where D – crystallite size (nm), K – Scherrer constant (~0.94 for spherical particles with a cubic symmetry), λ – the X-ray wavelength of Cu K-alpha (0.15406 nm), β – full width at half maximum, FWHM (gives line broadening in radians), and θ – Bragg angle.

$$D = \frac{0.94 \times 0.15406\ \text{nm}}{0.0431 \times \frac{\pi}{180} \times \cos\left(15.75 \times \frac{\pi}{180}\right)} = 200.02\ \text{nm}$$

This calculated crystallite size agrees with the observed size in TEM studies, as shown in Fig. S5 and S6.

Presence of polymorphism

Room-temperature and temperature-resolved SAXS measurements of the LC composites with different barium titanate loadings were employed to investigate the nanoscale structures present in the materials. For 0, 5, and 20 wt% $BaTiO_3$, the room-temperature SAXS profiles (Fig. 5) all exhibit two superposed families of reflections arising from layer-like structures. The first series exhibits a primary Bragg peak at q_A ($q_A = 0.141$ Å^{-1}) followed by a higher-order peak at $3q_A$. We interpret this as consistent with a layer-like structure, or lamellar order, in which the scattering at $2q_A$ is strongly suppressed due to form-factor effects associated with a symmetric electron-density profile. The d-spacing of this structure is calculated as $d_A = 2\pi/q_A = 2\pi/0.141$ Å^{-1} ≈ 4.46 nm. This dimension is roughly twice the length of a single cyanobiphenyl (CB12) mesogenic side chain (~2.5 nm from previous work),[44] which strongly suggests the formation of a smectic bilayer. In such a structure, the repeating unit is not a single layer of mesogens but a pair of layers. The second series exhibits scattering maxima with peak locations in a 1 : 2 ratio with the d-spacing $d_B = 2\pi/q_B = 2\pi/0.300$ Å^{-1} ≈ 2.09 nm ($q_B = 0.300$ Å^{-1}), which is consistent with the dimensions of a single layer of the sidechain mesogen. The presence of two distinct sets of periodic reflections, with non-commensurate fundamental q-values, indicates nanoscale phase coexistence, implying that the as-cast material is not a single, homogeneous mesophase but is instead a polymorphic system containing at least two different, well-ordered lamellar structures.

The temperature-controlled SAXS data, including the first heating and cooling cycles, show that q_B, q_C, and q_D appear and disappear simultaneously, suggesting that they originate from the same structure (Fig. 6). However, q_C and q_D are not readily indexed as higher-order lamellar reflections, and we therefore attribute them to additional electron-density correlations, likely associated with CNC-rich domains in the system. Upon heating the sample above 90 °C, the structure evolves from the bilayer structure (q_A, $3q_A$) to the monolayer-included structure (q_B, q_C, and q_D), which corresponds to the T_{LC2} transition observed in the DSC data. During the subsequent cooling cycle, the monolayer-based structure persists and the bilayer reflections do not re-emerge, even at room temperature, for both 0 and 20 wt% $BaTiO_3$. The bilayer structure is therefore identified as a kinetically trapped, metastable state, which could be formed during the process of hot pressing followed by rapid quench, while the other structures are in the thermodynamically stable state. Both exist simultaneously for the as-cast sample, so both series of peaks are shown in the RT SAXS data. Notably, varying the $BaTiO_3$ loading from 0 to 20 wt% does not fundamentally alter this polymorphic behavior or the nature of the thermal transition, indicating a robust self-assembly of the LCP matrix that successfully incorporates the nanoparticles without significant structural disruption.

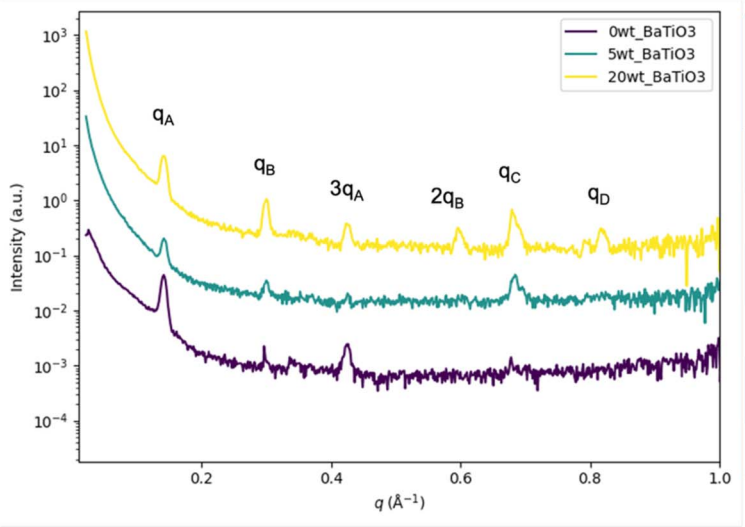

Peak Assignment	q values (A^{-1})	d-spacing (nm)
q_A	0.141	4.456
q_B	0.300	2.094
$3q_A$	0.423	1.485
$2q_B$	0.596	1.054
q_C	0.679	0.925
q_D	0.817	0.769

Fig. 5 Room temperature small-angle X-ray scattering (SAXS) results for the hybrid LCP and nanocomposites.

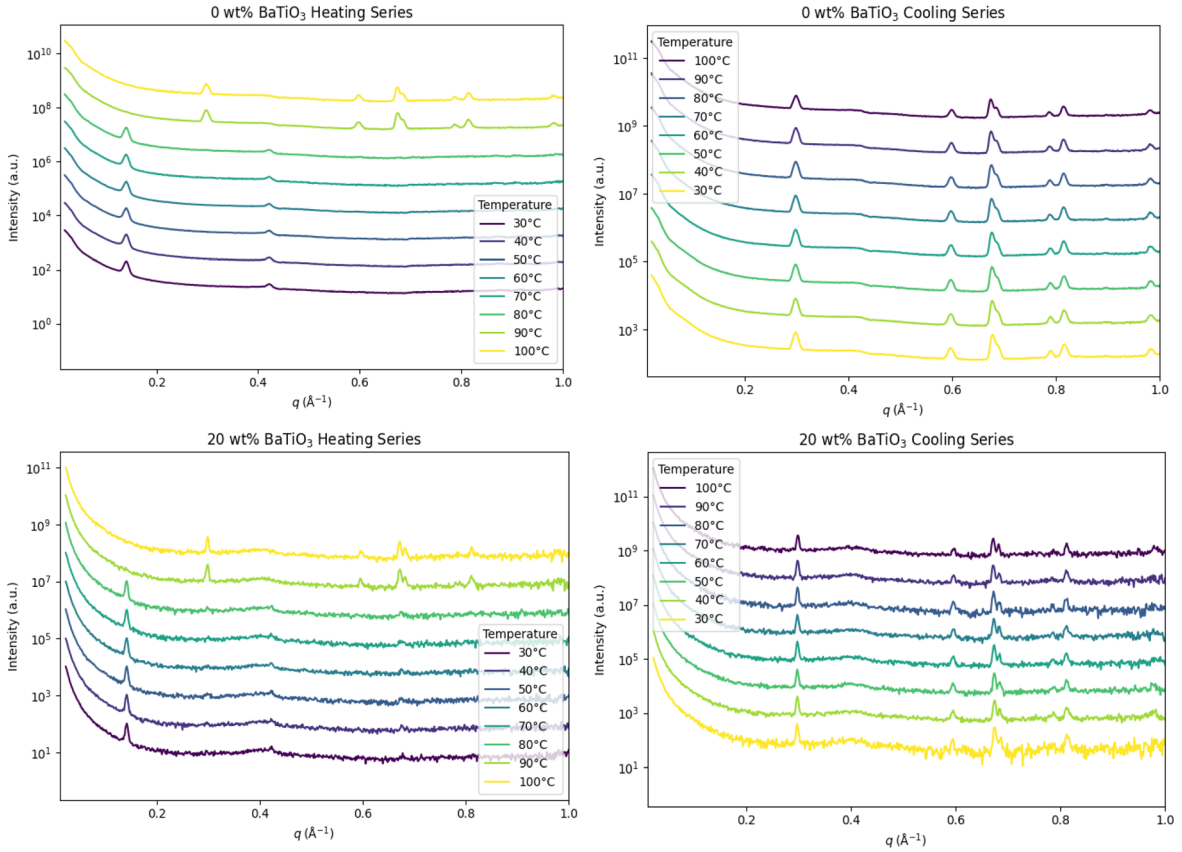

Fig. 6 Temperature resolved small-angle X-ray scattering (TSAXS) results for the hybrid LCP and nanocomposites.

Electronic structure analysis

The absorption intensity of the hybrid LCP and $BaTiO_3$/CNC-i-PA-ACB12-r-PAA nanocomposites is observed to increase sharply with the $BaTiO_3$ loading ratio, as shown in Fig. 7. Nanocomposites with a 40 wt% $BaTiO_3$ loading ratio had a maximum band gap energy of ~4.1 eV, which is about 20% more compared to the neat LCP. All the materials are non-conducting since their bandgap energy is higher than 3.0 eV.

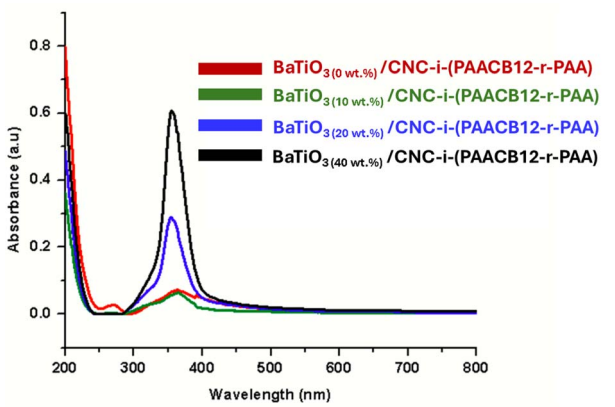

Fig. 7 UV-absorption results for the hybrid LCP (0 wt% $BaTiO_3$) and nanocomposites.

We also observe a distinct absorption peak at 275 nm, which corresponds to the π–π stacking resulting from cyanobiphenyl. At $BaTiO_3$ loading ratios of 20 wt% and 40 wt%, we observe a hypsochromic effect where the absorption peak appears blue-shifted from 375 nm relative to the 10 wt% nanocomposite and hybrid LCP. This proves that the $BaTiO_3$ concentration is vital when modifying the electrical behavior of dielectric nanocomposites. We therefore need to have a systematic balance between the intricate interplay between $BaTiO_3$, CB12, and CNCs. These bandgap energies are calculated from the λ_{max} using the equation below, and the results are summarized in Table 3.

$$E_g = \frac{hc}{\lambda}$$

where E_g is the bandgap energy, h – Planck's constant, c – speed of light ($\sim 3.0 \times 10^8$ m s^{-1}), and λ – wavelength (nm).

Table 3 Bandgap energies for the hybrid LCP and $BaTiO_3$/CNC-i-PAACB12-r-PAA nanocomposites with varying $BaTiO_3$ loading ratios

Nanocomposite	E_g (eV)
CNC-i-PAACB12-r-PAA	3.4
$BaTiO_3$ (10 wt%)/CNC-i-PAACB12-r-PAA	3.6
$BaTiO_3$ (20 wt%)/CNC-i-PAACB12-r-PAA	3.8
$BaTiO_3$ (40 wt%)/CNC-i-PAACB12-r-PAA	4.1

We observe that the LCP type has a significant impact on the electrical behavior of the nanocomposites. $BaTiO_3$/CNC nanocomposites appear more blue-shifted relative to $BaTiO_3$/PAACB12-r-PAA and $BaTiO_3$/CNC-i-PAACB12-r-PAA. Introduction of $BaTiO_3$ in CNC-i-PAACB12-r-PAA increases the absorption intensity of the material while impeding π–π stacking resulting from CB12 at 275 nm, as shown in Fig. 8.

Morphology

To understand the size of $BaTiO_3$ nanoparticles, we utilized transmission electron microscopy (TEM) studies.[45] Neat $BaTiO_3$ NPs were observed to have a quasi-spherical morphology, with an average particle size of about 200 nm as measured from a TEM micrograph (Fig. S6). This agreed with the calculated crystallite size calculated from XRD studies using the Scherrer equation. This shows that the particle size of the $BaTiO_3$ remained unchanged.

On the other hand, SEM studies offered complementary morphological insights into the nanoscale structural information obtained from TEM and X-ray studies.[45] SEM samples are sputtered with a 5 nm layer of 80/20 AuPd before the test. At 10 K magnification, SEM micrographs for $BaTiO_3$ (20 wt%)/CNC-i-PAACB12-r-PAA nanocomposites annealed at different LC transition temperatures (Fig. S7 and S8) showed a smooth CNC-LCP matrix with distributed particulate features, pertinent to the $BaTiO_3$ nanoparticles. We observe minor agglomeration clusters of about 100 nm in isolated regions and a layered texture, consistent with the smectic cyanobiphenyl polymer as confirmed by the SAXS scattering results. This layered texture also exhibited a fibrillated texture associated with CNC alignment. The partially agglomerated clusters appeared sparsely distributed, while most of the $BaTiO_3$ is embedded along the CNC-rich domains. This aligns with the SAXS evidence of smectic self-assembly of CNC-LCP nanocomposites, where CNCs provide the nucleation site for $BaTiO_3$ and act as a rigid template that influences LC molecular alignment. This templated dispersion minimizes random aggregation, resulting in a long-range order of the $BaTiO_3$ and mesogens, as observed in the room-temperature SAXS profile (Fig. 5). We note that bulk-level homogeneity cannot be confirmed without cross-sectional electron microscopy. However, the SEM results revealed the absence of interfacial voids between $BaTiO_3$ and the LCP, which correlates with the small domain analysis conducted by X-ray diffraction (XRD) studies, where the persistence of CNC and LC structural peaks after $BaTiO_3$ integration showed a retained crystalline order of the individual moieties. The inclusion of $BaTiO_3$ stabilized the thermal behavior of the nanocomposites, as confirmed by TGA studies (Fig. 2).

Dielectric performance

To investigate the impact of $BaTiO_3$ on the dielectric properties, broadband dielectric spectroscopy of both the CNC-i-PAACB12-r-PAA polymer matrix and $BaTiO_3$ (20 wt%)/CNC-i-PAACB12-r-PAA nanocomposites is performed. As shown in Fig. 9(a)–(d), the dielectric constant (ε) and loss of the polymer matrix and nanocomposite become significantly large at relatively high temperatures (>0 °C) and low frequencies, indicating considerable contributions from electrode polarization (EP) and D.C. conductivity. At 10 kHz, the ε of CNC-i-PAACB12-r-PAA is 5.9 at −30 °C and 8.1 at 30 °C, whereas the nanocomposite reaches 8.2 and 10.8, potentially due to the Maxwell–Wagner-Sillars polarization at the $BaTiO_3$–polymer interface.

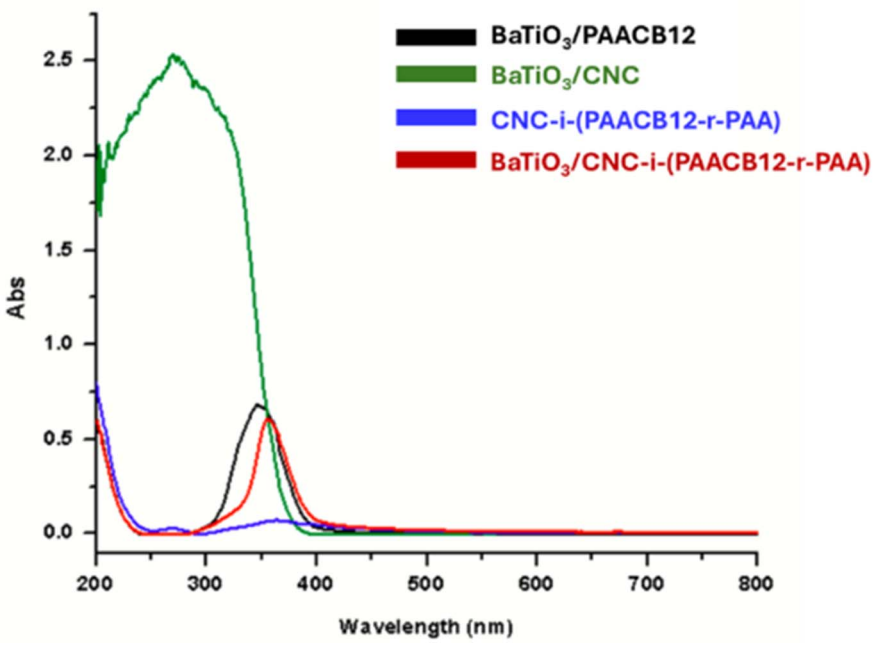

Fig. 8 UV-absorption results for the hybrid LCP and nanocomposites.

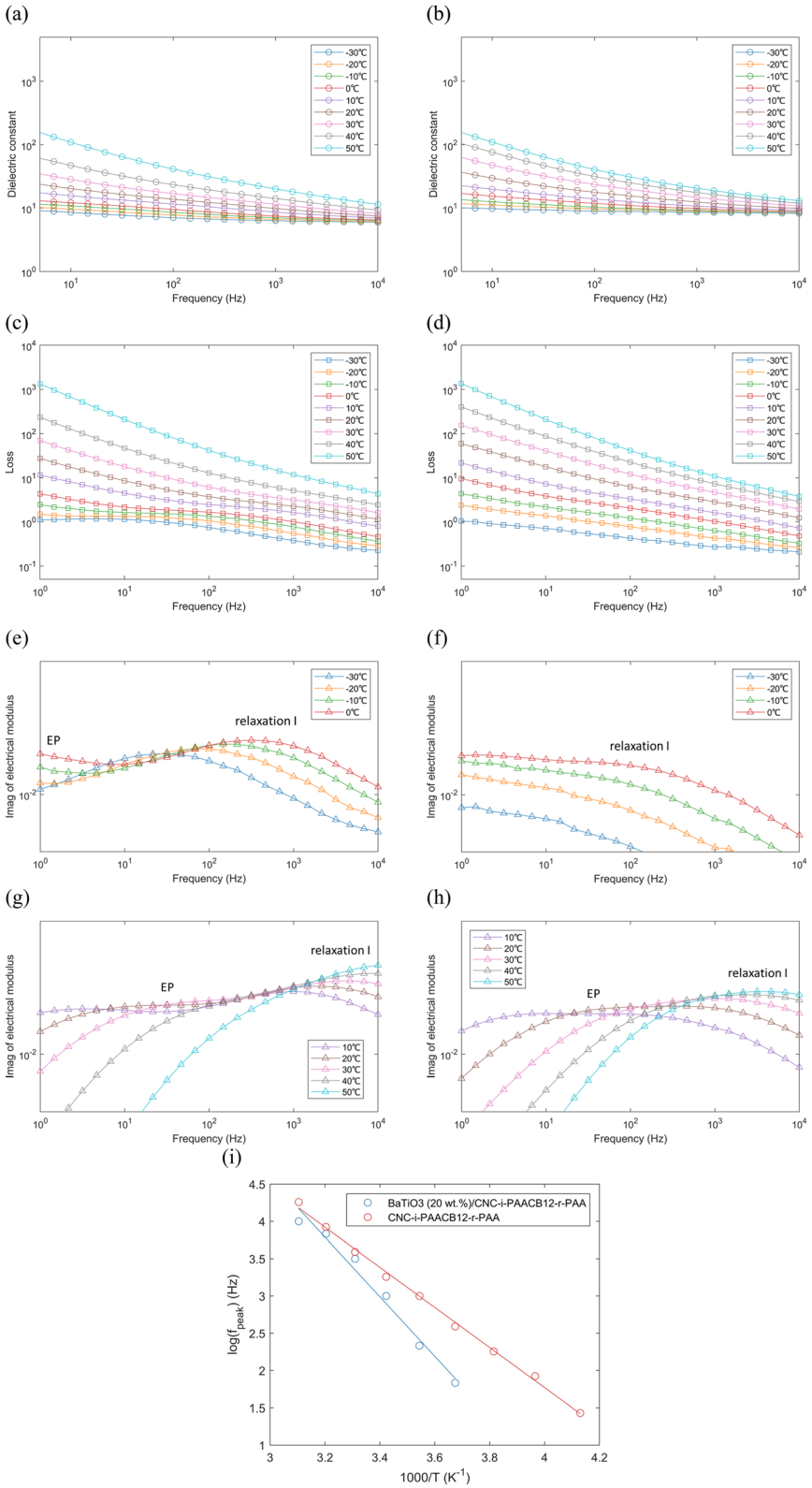

Fig. 9 Broadband dielectric spectra of CNC-i-PAACB12-r-PAA and $BaTiO_3$ (20 wt%)/CNC-i-PAACB12-r-PAA nanocomposites. Dielectric constant of (a) CNC-i-PAACB12-r-PAA and (b) $BaTiO_3$ (20 wt%)/CNC-i-PAACB12-r-PAA nanocomposites. Loss of (c) CNC-i-PAACB12-r-PAA and (d) $BaTiO_3$ (20 wt%)/CNC-i-PAACB12-r-PAA nanocomposites. The imaginary component of the electrical modulus of CNC-i-PAACB12-r-PAA (e) from −30 °C to 0 °C and (g) from 0 °C to 50 °C. The imaginary component of the electrical modulus of $BaTiO_3$ (20 wt%)/CNC-i-PAACB12-r-PAA nanocomposites (f) from −30 °C to 0 °C and (h) from 0 °C to 50 °C. (i) Arrhenius plot of both materials (blue for CNC-i-PAACB12-r-PAA; orange for $BaTiO_3$ (20 wt%)/CNC-i-PAACB12-r-PAA nanocomposites).

The effect of $BaTiO_3$ on relaxation dynamics is further examined *via* the imaginary part of the electrical modulus, $M^*(\omega) = 1/\varepsilon^*(\omega)$. As illustrated in Fig. 9(e)–(h), both the polymer matrix and the nanocomposite display two loss peaks in their imaginary M^*. The loss peaks appearing in the very low frequency range, where ε of both materials significantly increases, are EP-induced relaxation processes. The low-frequency EP loss peak of the nanocomposite overlaps more with its high-frequency peak compared to the polymer matrix (Fig. 9(e)–(h)), which is attributed to the increased D.C. conductivity due to the incorporation of $BaTiO_3$, thus reducing the time constant of the EP relaxation process.[46,47] The high-frequency peak, observed in the imaginary M^* of both materials (not in the nanocomposite alone), is associated with the dielectric response of the polymer matrix rather than the $BaTiO_3$-polymer interfacial polarization. This is further supported by the fact that the high-frequency loss peak is still observed in PAACB12-r-PAA without CNC interlocking (Fig. S9). Since the dielectric spectroscopy measurement is conducted at T_{LC1}, the observed relaxation process should be attributed to the β process due to the librational fluctuations of the mesogen (12-spacer cyanobiphenyl) around the long molecular axis (carboxyl groups are largely fixed due to hydrogen bonding with CNCs). Arrhenius plots in Fig. 9(g) demonstrate the temperature-dependent relaxation rates ($1/\tau_{peak}$) of this relaxation process for both materials. The relaxation process of the nanocomposite possesses a higher activation energy and a slower relaxation rate compared to the polymer matrix, implying a suppressed relaxation process due to the presence of $BaTiO_3$ nanoparticles. A traditional reason for restricted relaxation in nanocomposite polymers is the attraction at the interface between inorganic nanoparticles and the polymer matrix.[48] However, in the LCP nanocomposite, $BaTiO_3$ and CNC-i-PAACB12-r-PAA do not form a classical thermodynamically wetted interface. In contrast, the presence of interfacial adhesion, mediated by dipolar and surface interactions, strengthens the proposed mechanism: restricted mesogen mobility arises from interfacial anchoring and ordering constraints imposed by the $BaTiO_3$ surface, rather than from a fully wetted or chemically bonded interface.

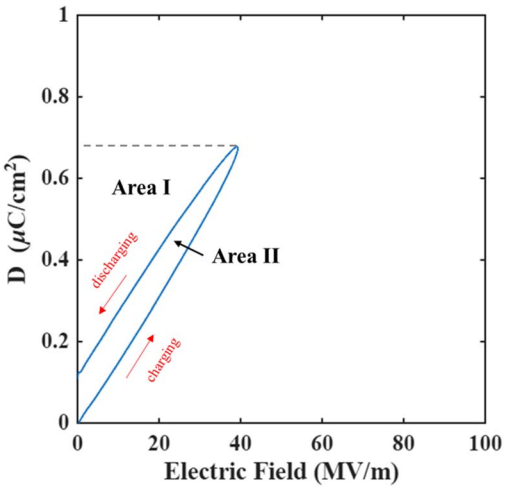

Fig. 11 *D*–*E* loops for $BaTiO_3$(20 wt%)/CNC-i-PAACB12-r-PAA nanocomposites.

Therefore, $BaTiO_3$ nanoparticles primarily function as a steric hindrance while facilitating the formation of a long-range ordered structure, thereby reducing the mobility of the mesogen. Due to this restricted movement of the mesogen, the liquid–crystal transition temperature (T_{LC1}) of the nanocomposite is also slightly increased.

Due to the exceptionally high dielectric constant of $BaTiO_3$(20 wt%)/CNC-i-PAACB12-r-PAA nanocomposites, which exceeds that of state-of-the-art commercial capacitor-grade film (BOPP) by more than four-fold, a discharge energy density of 0.1 J cm^{-3} has already been achieved at only ~40 MV m^{-1}, Fig. 10. Given the relatively large sample thickness, electrical breakdown did not occur even after the maximum voltage of our power supply (10 kV) was applied, which limits the experimental evaluation of discharge energy density at higher electric fields.

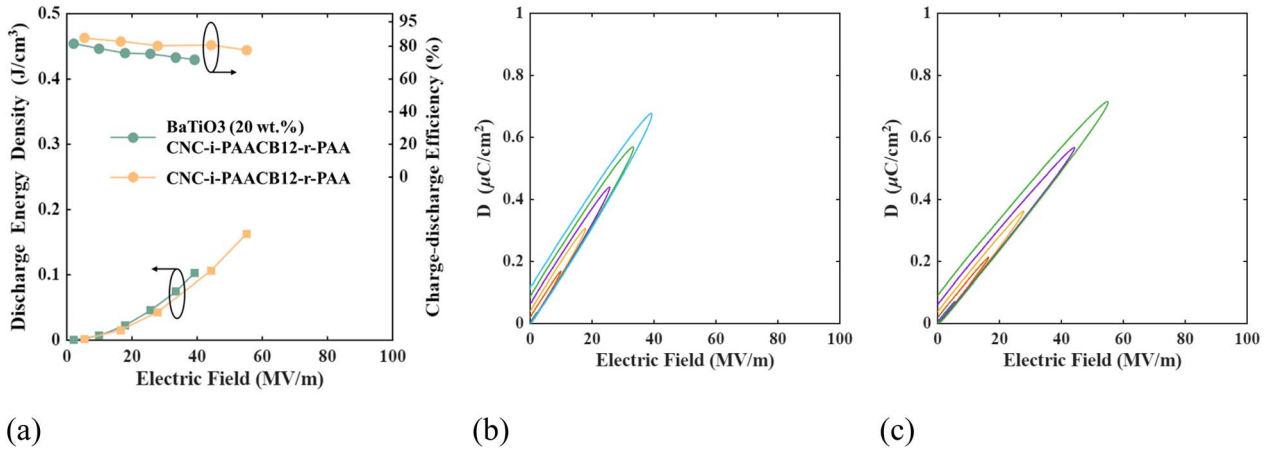

Fig. 10 Displacement–electric field (*D*–*E*) loop of $BaTiO_3$(20 wt%)/CNC-i-PAACB12-r-PAA nanocomposites and CNC-i-PAACB12-r-PAA. (a) Discharge energy density and charge–discharge efficiency of $BaTiO_3$(20 wt%)/CNC-i-PAACB12-r-PAA nanocomposites and CNC-i-PAACB12-r-PAA below 100 MV m^{-1}. The *D*–*E* loop of (b) $BaTiO_3$(20 wt%)/CNC-i-PAACB12-r-PAA nanocomposites and (c) CNC-i-PAACB12-r-PAA.

However, based on theoretical estimation using dielectric constant, the discharge energy density of $BaTiO_3$(20 wt%)/CNC-i-PAACB12-r-PAA nanocomposites can reach approximately 2.2 J cm^{-3} at 200 MV m^{-1} (the typical design field of BOPP), assuming a 70% charge–discharge efficiency. In comparison, BOPP delivers a 0.39 J cm^{-3} at 200 MV m^{-1}.[49] The *D–E* loop of $BaTiO_3$(20 wt%)/CNC-i-PAACB12-r-PAA nanocomposites and CNC-i-PAACB12-r-PAA are presented in Fig. 10.

The energy storage behavior of dielectric materials can be described by the following equations. As illustrated in the D-E loop in Fig. 11, the charged energy density corresponds to the total area of Area I and Area II, whereas the discharged energy density is represented by Area I alone. Therefore, minimizing Area II, which reflects energy loss, is essential for achieving high charge–discharge efficiency and maximizing discharge energy density.

$$U_e = \int EdD = \text{Area}_I$$

$$U_{loss} = \text{Area}_{II}$$

$$\eta = \frac{\text{Area}_{II}}{\text{Area}_I + \text{Area}_{II}} \times 100\%$$

where U_e: discharged energy density, U_{loss}: loss, E: electric field, D: electric displacement, Area_I: area of Area I, Area_{II}: area of Area II, and η: charge–discharge efficiency.

Conclusion

We successfully designed a novel hybrid energy storage material comprising $BaTiO_3$-loaded CNC/LCP nanocomposites and conducted a comprehensive structure–property evaluation, including mesophase behavior. The correlation between self-assembled mesostructures and dielectric performance was systematically established. Compression molding of $BaTiO_3$-loaded CNC/LCP nanocomposite films promoted the ordering of liquid crystals (LCs) around the $BaTiO_3$ nanoparticles, enabling long-range organization without the need for external field-induced alignment. LC–LC interactions were found to dominate the system, leading to mesostructures consistent with the smectic mesophase associated with the CB12 mesogen.

Broadband dielectric spectroscopy performed on CNC-i-PAACB12-r-PAA and $BaTiO_3$ (20 wt%)/CNC-i-PAACB12-r-PAA samples revealed a significant increase in the dielectric constant (ε) and loss at temperatures above 0 °C and low frequencies, attributed to electrode polarization (EP) and DC conductivity. These effects diminished above 10 kHz, consistent with Kramers–Kronig analysis. The ε values increased from 5.9 to 8.1 (−30 °C to 30 °C) for the CNC-i-PAACB12-r-PAA hybrid polymer and from 8.2 to 10.8 for the $BaTiO_3$ (20 wt%) nanocomposite. This enhancement is attributed to Maxwell–Wagner–Sillars polarization at the $BaTiO_3$–polymer interface. Overall, the dielectric response is strongly governed by LCP molecular alignment and interfacial polarization effects. Variations in relative permittivity and loss tangent further highlight the role of CNC interlocking in promoting uniform morphology and retaining structural integrity of the films.

Relaxation dynamics, analyzed *via* the imaginary part of the electrical modulus ($M^*(\omega)$), revealed two distinct loss peaks in both systems. The low-frequency peak, associated with EP relaxation, overlapped with the high-frequency peak in the nanocomposite due to enhanced DC conductivity from $BaTiO_3$, resulting in reduced EP relaxation time. The high-frequency peak originated from the polymer matrix dielectric response, as confirmed by its presence in PAACB12-r-PAA without CNC interlocking. The relaxation mechanism corresponds to mesogen (CB12) β-process fluctuations, with Arrhenius analysis indicating clear temperature dependence. Compared to the polymer matrix, the nanocomposite exhibited higher activation energy, a slower relaxation rate, and an increased liquid–crystal transition temperature (T_{LC}), consistent with restricted side-chain mobility induced by $BaTiO_3$ nanoparticles, in agreement with the DSC results.

Overall, the incorporation of $BaTiO_3$ into CNC-based cyanobiphenyl LCP nanocomposites enhances domain ordering and interfacial polarization, leading to improved dielectric performance. While the observed morphology suggests good structural integrity upon filler incorporation, quantitative evaluation of mechanical properties such as toughness and brittleness requires further investigation. Nevertheless, the synergistic integration of LCP ordering, CNC reinforcement, and $BaTiO_3$ highlights the strong potential of this nanocomposite system for next-generation energy storage applications, particularly capacitors with tunable dielectric properties enabled by controlled molecular design and self-assembly.

Conflicts of interest

The authors declare no conflict of interest.

Data availability

All the data reported in this manuscript are available in tables and figures both in the main manuscript and the supplementary information (SI). Supplementary information is available. See DOI: https://doi.org/10.1039/d6ta00808a.

Acknowledgements

P. K. N. and the authors remain indebted to Dr Sun Xuanhao of the Bioscience Electron Microscopy Laboratory and Dr Lichun Zhang of the Center for Advanced Microscopy and Materials Analysis (CAMMA) at the Innovation Partnership Building (IPB) for their assistance. R. M. K. is grateful for support from NSF through DMR-1507045 and the University of Connecticut Office of the Vice President for Research (OVPR) Research Excellence Program. N. G. and Y. C. would like to acknowledge the support of the Office of Naval Research (N0014-23-1-2062). C. O. and H. L. acknowledge NSF support through DMR 2223705. We also acknowledge the central instrumentation facilities within the Institute of Materials Science and the Department of Chemistry, including instrumentation in the laboratory of Prof. Steven

Suib, and the small-angle X-ray scattering facilities at the University of Pennsylvania. Finally, we thank Prof. Menka Jain and her students for valuable discussions.

References

1 M. Yang, M. Guo, E. Xu, W. Ren, D. Wang, S. Li, S. Zhang, C.-W. Nan and Y. Shen, Polymer nanocomposite dielectrics for capacitive energy storage, *Nat. Nanotechnol.*, 2024, **19**(5), 588–603.

2 F. Faheem, M. Arsalan and M. E. Khan, Recent developments of nanocomposites in energy-related applications, *Nanocomposites-Advanced Materials for Energy and Environmental Aspects*, 2023, pp. 111–127.

3 Q.-K. Feng, S.-L. Zhong, J.-Y. Pei, Y. Zhao, D.-L. Zhang, D.-F. Liu, Y.-X. Zhang and Z.-M. Dang, Recent progress and future prospects on all-organic polymer dielectrics for energy storage capacitors, *Chem. Rev.*, 2021, **122**(3), 3820–3878.

4 D. Vignesh and E. Rout, Multipurpose Polymer Dielectric Materials and Composites for Advanced Energy Applications, in *Metal Oxide-Based High-K Dielectrics*, CRC Press, 2025, pp 289–332.

5 Y. Wang, M. Yao, R. Ma, Q. Yuan, D. Yang, B. Cui, C. Ma, M. Liu and D. Hu, Design strategy of barium titanate/polyvinylidene fluoride-based nanocomposite films for high energy storage, *J. Mater. Chem. A*, 2020, **8**(3), 884–917.

6 L. You, B. Liu, H. Hua, H. Jiang, C. Yin and F. Wen, Energy storage performance of polymer-based dielectric composites with two-dimensional fillers, *Nanomaterials*, 2023, **13**(21), 2842.

7 J. Chen, X. Liu, Y. Tian, W. Zhu, C. Yan, Y. Shi, L. B. Kong, H. J. Qi and K. Zhou, 3D-Printed anisotropic polymer materials for functional applications, *Adv. Mater.*, 2022, **34**(5), 2102877.

8 M. M. Mhatre, A. Katariya-Jain, M. H. Saeed and R. Deshmukh, Effects of multifunctional thiol monomers and BaTiO3 nanoparticles on electro-optical and dielectric properties of polymer dispersed liquid crystal films, *J. Mol. Liq.*, 2024, **413**, 125945.

9 W. Wu, X. Sun, D. Wang, H. Qian, B. Wang, X. Wang, X. Rong, X. Zhang and G. Wu, The effect of high dielectric BaTiO 3 nanoparticle dimensions on the dielectric properties and electro-optical performance of polymer dispersed liquid crystal films, *J. Mater. Chem. C*, 2024, **12**(20), 7386–7397.

10 D. Zhang, C. Ma, X. Zhou, S. Chen, H. Luo, C. R. Bowen and K. Zhou, High performance capacitors using BaTiO3 nanowires engineered by rigid liquid-crystalline polymers, *J. Mater. Chem. C*, 2017, **121**(37), 20075–20083.

11 Y. B. Adediji, A. M. Adeyinka, D. I. Yahya and O. V. Mbelu, A review of energy storage applications of lead-free BaTiO3-based dielectric ceramic capacitors, *Energy, Ecol. Environ.*, 2023, **8**(5), 401–419.

12 D. Hu, Z. Pan, X. Tan, F. Yang, J. Ding, X. Zhang, P. Li, J. Liu, J. Zhai and H. Pan, Optimization the energy density and efficiency of BaTiO3-based ceramics for capacitor applications, *Chem. Eng. J.*, 2021, **409**, 127375.

13 C. Deng, Y. Zhang, D. Yang, H. Zhang and M. Zhu, Recent progress on barium titanate-based ferroelectrics for sensor applications, *Adv. Sens. Res.*, 2024, **3**(6), 2300168.

14 Prateek, V. K. Thakur and R. K. Gupta, Recent progress on ferroelectric polymer-based nanocomposites for high energy density capacitors: synthesis, dielectric properties, and future aspects, *Chem. Rev.*, 2016, **116**(7), 4260–4317.

15 S. Wang, C. Yang, X. Li, H. Jia, S. Liu, X. Liu, T. Minari and Q. Sun, Polymer-based dielectrics with high permittivity and low dielectric loss for flexible electronics, *J. Mater. Chem. C*, 2022, **10**(16), 6196–6221.

16 H. Tao, M. Yan, L. Zhang, Z. Zou, B. Han, H. Dong, B. Zhu and X. Li, Progress in preparation, processing, and application of high dielectric polypropylene matrix composite materials, *Polym. Compos.*, 2024, **45**(6), 4819–4838.

17 G. Zhang, Q. Li, E. Allahyarov, Y. Li and L. Zhu, Challenges and opportunities of polymer nanodielectrics for capacitive energy storage, *ACS Appl. Mater. Interfaces*, 2021, **13**(32), 37939–37960.

18 Y. Jin, N. Xia and R. A. Gerhardt, Enhanced dielectric properties of polymer matrix composites with BaTiO3 and MWCNT hybrid fillers using simple phase separation, *Nano Energy*, 2016, **30**, 407–416.

19 A. Bouhamed, N. Jöhrmann, S. Naifar, B. Böhm, O. Hellwig, B. Wunderle and O. Kanoun, Collaborative filler network for enhancing the performance of BaTiO3/PDMS flexible piezoelectric polymer composite nanogenerators, *Sensors*, 2022, **22**(11), 4181.

20 J. Su and J. Zhang, Recent development on modification of synthesized barium titanate (BaTiO3) and polymer/BaTiO3 dielectric composites, *J. Mater. Sci.: Mater. Electron.*, 2019, **30**(3), 1957–1975.

21 S. Guo, X. Duan, M. Xie, K. C. Aw and Q. Xue, Composites, fabrication and application of polyvinylidene fluoride for flexible electromechanical devices: A review, *Micromachines*, 2020, **11**(12), 1076.

22 L. Li, L. Han, H. Hu and R. Zhang, A review on polymers and their composites for flexible electronics, *Mater. Adv.*, 2023, **4**(3), 726–746.

23 X. Hu, A. K. An and S. S. Chopra, Life cycle assessment of the polyvinylidene fluoride polymer with applications in various emerging technologies, *ACS Sustain. Chem. Eng.*, 2022, **10**(18), 5708–5718.

24 B. Améduri and H. Hori, Recycling and the end of life assessment of fluoropolymers: recent developments, challenges and future trends, *Chem. Soc. Rev.*, 2023, **52**(13), 4208–4247.

25 B. Ameduri, From vinylidene fluoride (VDF) to the applications of VDF-containing polymers and copolymers: recent developments and future trends, *Chem. Rev.*, 2009, **109**(12), 6632–6686.

26 D. Ji, M. Zhang, H. Sun, B. Yuan, C. Ma, Z. He, Y. Ni and S. Song, Enhanced mechanical and dielectric properties of lignocellulosic composite papers with biomimetic

multilayered structure and multiple hydrogen-bonding interactions, *Int. J. Biol. Macromol.*, 2024, **281**, 136247.
27 Z. Du, N. Wang and J. Du, Recent Progress in Cellulose-Based Conductive Hydrogels, *Polymers*, 2025, **17**(8), 1089.
28 G. Du, J. Wang, Y. Liu, J. Yuan, T. Liu, C. Cai, B. Luo, S. Zhu, Z. Wei and S. Wang, Fabrication of advanced cellulosic triboelectric materials via dielectric modulation, *Advanced Science*, 2023, **10**(15), 2206243.
29 J. Jose, J. A. Salam and V. Thomas, Effect of temperature and frequency on the dielectric behaviour of cellulose nanocrystals, *Ind. Crops Prod.*, 2024, **222**, 119428.
30 L. Zhou, S. Liu, X. Miao, P. Xie, N. Sun, Z. Xu, T. Zhong, L. Zhang and Y. Shen, Advancements and applications of liquid crystal/polymer composite films, *ACS Mater. Lett.*, 2023, **5**(10), 2760–2775.
31 J. Guardia, J. A. Reina, M. Giamberini and X. Montane, An up-to-date overview of liquid crystals and liquid crystal polymers for different applications: a review, *Polymers*, 2024, **16**(16), 2293.
32 F. K. Masese, P. K. Njenga, D. M. Ndaya and R. M. Kasi, Recent advances and opportunities for cellulose nanocrystal-based liquid crystalline polymer hybrids and composite materials, *Macromolecules*, 2023, **56**(17), 6567–6588.
33 S. Jia, B. Yang, J. Du, Y. Xie, L. Yu, Y. Zhang, T. Tao, W. Tang and J. Gong, Uncovering the Recent Progress of CNC-Derived Chirality Nanomaterials: Structure and Functions, *Small*, 2024, **20**(35), 2401664.
34 A. Abbasi Moud, Chiral liquid crystalline properties of cellulose nanocrystals: fundamentals and applications, *ACS Omega*, 2022, **7**(35), 30673–30699.
35 R. K. Mishra, A study of control mechanisms in micro and nano system-enhanced polymer nanocomposites under mechanical and electrical stimuli, *An Experimental and Computational Investigation*, Cranfield University, 2023.
36 B. S. Sahoo, N. K. Nath, R. Parida, B. N. Parida and N. C. Nayak, Dielectric Behaviour and Energy Storage Performance of La-Doped GdFeO3 Nanoparticle Filled PVDF Composite, *Ceram. Int.*, 2025, 54244–54254.
37 R. Guo, H. Luo, M. Yan, X. Zhou, K. Zhou and D. Zhang, Significantly enhanced breakdown strength and energy density in sandwich-structured nanocomposites with low-level BaTiO3 nanowires, *Nano Energy*, 2021, **79**, 105412.
38 Q. Luo, Y. Liu, G. Zhou and X. Xu, A new strategy to improve the dielectric properties of cellulose nanocrystals (CNCs): Surface modification of small molecules, *Carbohydr. Polym.*, 2024, **324**, 121451.
39 A. Babaei-Ghazvini and B. Acharya, The effects of aspect ratio of cellulose nanocrystals on the properties of all CNC films: Tunicate and wood CNCs, *Carbohydr. Polym. Technol. Appl.*, 2023, **5**, 100311.
40 A. Durairaj, M. Maruthapandi, A. Saravanan, J. H. Luong and A. Gedanken, Cellulose nanocrystals (CNC)-based functional materials for supercapacitor applications, *Nanomaterials*, 2022, **12**(11), 1828.
41 N. F. A. Zainal, J. M. Saiter, S. I. A. Halim, R. Lucas and C. H. Chan, Thermal analysis: basic concept of differential scanning calorimetry and thermogravimetry for beginners, *Chem. Teach. Int.*, 2021, **3**(2), 59–75.
42 D. Lőrinczy, A. Bata, Z. Lábas, F. Shafiei, H. Szabó, J. Cifra and L. G. Nöt, Thermal analysis of tendon, cartilage and bone samples from shoulder joint replacement patients using differential scanning calorimetry (DSC) and thermogravimetry (DTA/TG), *J. Therm. Anal. Calorim.*, 2024, **149**(20), 11471–11483.
43 C. Bracht, T. Preitschopf, M. Schöneich, T. Neff, C. Kallfaß and M. Finze, Influence of Crucible Types on Thermal Stability Analysis of Li-Ion Battery Components by Thermogravimetric Analysis–Differential Scanning Calorimetry, *Energy Technol.*, 2024, **12**(8), 2400365.
44 F. K. Masese, D. Ndaya, C.-H. Liu, N. Eddy, M. D. Morales-Acosta, M.-P. Nieh and R. M. Kasi, Self-assembled materials from cellulose nanocrystals conjugated with a thermotropic liquid crystalline moiety, *Soft Matter*, 2022, **18**(42), 8165–8174.
45 T. Yu, X. Ji, Z. Fu, B. Xia, S. Jiang and M. Gao, Morphology, structure, and defect design of BaTiO3-based ceramics for optimizing energy storage performance, *J. Alloys Compd.*, 2025, **1026**, 180220.
46 F. Kremer and A. Schönhals, *Broadband Dielectric Spectroscopy*, Springer Science & Business Media, 2002.
47 W. H. Woodward Broadband dielectric spectroscopy—A practical guide, in *Broadband Dielectric Spectroscopy: A Modern Analytical Technique*, ACS Publications, 2021, pp 3–59.
48 S. K. Sharma, J. Prakash, J. Bahadur, M. Sahu, S. Mazumder and P. K. Pujari, Free volume and lamellar structure of poly vinyl alcohol-nanosized BaTiO3 composite: positron annihilation and small angle X-ray scattering study, *Eur. Polym. J.*, 2016, **84**, 100–110.
49 Z. Dai, Z. Bao, S. Ding, C. Liu, H. Sun, H. Wang, X. Zhou, Y. Wang, Y. Yin and X. Li, Scalable polyimide-poly (amic acid) copolymer based nanocomposites for high-temperature capacitive energy storage, *Adv. Mater.*, 2022, **34**(5), 2101976.

